Journal of
Ship&Ocean
Technology
© MARCH 2001

SOTECH Vol. 5, No. 1, pp. 38~54, 2001

Simulation of Turbulent Flow and Surface Wave Fields around Series 60 C_B=0.6 Ship Model

Hyoung-Tae Kim[1] and Jung-Joong Kim[2]

[1]Chungnam National University, Taejon, KOREA 305-764; E-mail: h-tkim@cnu.ac.kr
[2]Samsung Heavy Industries Co., Ltd. Shipbuilding Plant Research Institute P.O. Box 43, Daeduk Science Town, Taejon, KOREA 305-600

Abstract

A finite difference method for calculating turbulent flow and surface wave fields around a ship model is evaluated through the comparison with the experimental data of the Series 60 $C_B = 0.6$ ship model. The method solves the Reynolds-averaged Navier-Stokes Equations using the non-staggered grid system, the four-stage Runge-Kutta scheme for the temporal integration of governing equations and the Baldwin-Lomax model for the turbulence closure. The free surface waves are captured by solving the equation of the kinematic free-surface condition using the Lax-Wendroff scheme and free-surface conforming grids are generated at each time step so that one of the grid surfaces coincides always with the free surface. The computational results show an overall close agreement with the experimental data and verify that the present method can simulate well the turbulent boundary layers and wakes as well as the free-surface waves.

Keywords: RANS equations, turbulent flow, free-surface wave, finite difference method

1 Introduction

During the last fifteen years, there has been a significant progress in the development of the Reynolds-averaged Navier-Stokes(RANS) equation method for computing the viscous flow field around a surface ship model including the free surface waves. CFD Workshop Tokyo(1994) typically showed recent developments in this area. In the workshop, the computational results of various RANS solvers were comparably evaluated through the comparison with the experimental data for the Series 60 $C_B = 0.6$ ship model. The results could be summarized as follows. The pressures on the hull surface were generally in good agreements with the measurements, but not the shear stresses. The velocities were in fair agreements with the data, but the discrepancies among the computations were not small. The hull-side wave profiles were in good agreements, but the computed wave contours did not match with the measured data particularly in the far field. Lastly, the resistance was not accurately predicted. Perhaps the most important issue reiterated in the workshop was the relative importance of errors due to inaccurate numerical scheme, insufficient grid resolution and defective turbulence model. The present situation is not quite different from the time of the workshop. Being premature to replace the model test in the towing tank,

RANS methods for calculating viscous flow and wave fields around a ship model would become a powerful tool for hull-form design if the accuracy of the results were improved a bit further. More accurate RANS solvers are still in need. The object of the present paper is to evaluate the RANS solver of Kim and Kim(2000) through comparisons of the computational results with the experimental data of the Series 60 $C_B = 0.6$ ship model for non-zero Froude number. In what follows, the governing equations and the numerical methods are briefly prescribed. Then, the results are presented in comparisons with the experimental data and finally some conclusions are made together with future works.

2 Governing equations

The governing equations are the incompressible RANS equations which describe the conservation of mass and momentum and can be written in the Cartesian tensor notation as follows:

- Continuity equation

$$\frac{\partial u_k}{\partial x_k} = 0 \tag{1}$$

- Momentum equations

$$\frac{\partial u_i}{\partial t} + u_j \frac{\partial u_i}{\partial x_j} = -\frac{\partial}{\partial x_i}\left(p - \frac{z}{F_r^2}\right) + \frac{1}{Re}\frac{\partial^2 u_i}{\partial x_j \partial x_j} + \frac{\partial}{\partial x_j}\left[-\overline{u_i' u_j'}\right] \tag{2}$$

where $x_i = (x, y, z)$, $u_i = (u, v, w)$, $-\overline{u_i' u_j'}$ denotes the Reynolds stresses and the summation convention is used. The equations are normalized by a ship length L, the ship speed V_s, the fluid density ρ and the viscosity μ. The Reynolds number and Froude number are defined by $R_e = \frac{V_s L}{\nu}$ and $F_r = \frac{V_s}{\sqrt{gL}}$ respectively, where ν is the kinematic viscosity and g is the gravitational acceleration. For the turbulence closure, the Boussinesq-isotropic-turbulence hypothesis is implemented and the Reynolds stresses can be written as follows:

$$-\overline{u_i' u_j'} = \nu_t \left(\frac{\partial u_i}{\partial x_j} + \frac{\partial u_j}{\partial x_i}\right) - \frac{2}{3}\delta_{ij}\mathrm{k} \tag{3}$$

where δ_{ij} is the Kronecker delta function and k is the turbulent kinetic energy. Thus, the mean momentum equations with an isotropic eddy viscosity model are

$$\frac{\partial u_i}{\partial t} + u_j \frac{\partial u_i}{\partial x_j} = -\frac{\partial}{\partial x_i}(P) + \frac{\partial}{\partial x_j}(\nu_e \tau_{ij}) \tag{4}$$

where, $\nu_e = 1/R_e + \nu_t$, $P = p - \frac{z}{F_r^2} + \frac{2}{3}\mathrm{k}$ and $\tau_{ij} = \left(\frac{\partial u_i}{\partial x_j} + \frac{\partial u_j}{\partial x_i}\right)$
Equation (1) and (4) can be solved for u_i and P when the eddy viscosity ν_t is provided by a suitable turbulence model. In the present study, the eddy viscosity is obtained using a modified Baldwin-Lomax model of Chiema et al(1993) with a correction to the outer eddy viscosity for the

thick boundary layer(Sung et al, 1993) in the stern region where the boundary layer thickness δ is greater than 15% of the local radius $r_0 = \sqrt{A(x)/\pi}$ in which $A(x)$ is the section area of the hull.

The governing equations in the physical space (x, y, z) are to be transformed into those in the computational domain (ξ, η, ζ). See the physical and computational domains in Figure 1.

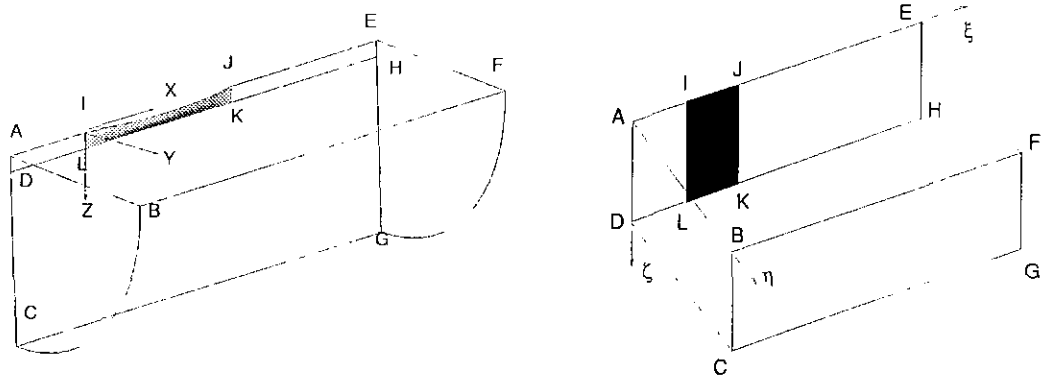

Figure 1: Physical and computational domains and coordinate system

In the present study, the partial transformation is employed so that only coordinates are transformed while the velocity is left in Cartesian coordinates. As the free surface elevation is calculated by solving the equation of the kinematic condition at each time step, the updated free surface position is used to regenerate a moving boundary fitted grid. The so-called "grid velocity" was considered in the present method. The governing equations in generalized coordinates are as follows:

o Continuity equation

$$J \frac{\partial}{\partial \xi^k} \left(\frac{U^k}{J} \right) = 0 \tag{5}$$

o Momentum equations

$$\frac{\partial u_i}{\partial t} + U^k \frac{\partial u_i}{\partial \xi^k} + \xi^k_{x_i} \frac{\partial}{\partial \xi^k} P - J \left(\frac{\partial E_{v1}}{\partial \xi} + \frac{\partial E_{v2}}{\partial \eta} + \frac{\partial E_{v3}}{\partial \zeta} \right) = 0 \tag{6}$$

where $J \left(= \frac{\partial(\xi,\eta,\zeta)}{\partial(x,y,z)} \right)$ represents the Jacobian of transformation and the contravariant velocity components and grid velocity are defined by $U^k = \xi^k_{x_j}(u_j + \frac{\partial x^j_g}{\partial t})$. $\frac{\partial x^j_g}{\partial t}$ represents the grid velocity. The E_{v1}, E_{v2}, E_{v3} in the equation (6) are the viscous flux vectors defined as follows :

$$E_{vj} = \frac{\nu_t}{J} \times \begin{bmatrix} (\xi_x \xi^j_x + g^{1j})u_\xi + (\eta_x \xi^j_x + g^{2j})u_\eta + (\zeta_x \xi^j_x + g^{3j})u_\zeta + S_{1j} \\ (\xi_y \xi^j_y + g^{1j})v_\xi + (\eta_y \xi^j_y + g^{2j})v_\eta + (\zeta_y \xi^j_y + g^{3j})v_\zeta + S_{2j} \\ (\xi_z \xi^j_z + g^{1j})w_\xi + (\eta_z \xi^j_z + g^{2j})w_\eta + (\zeta_z \xi^j_z + g^{3j})w_\zeta + S_{3j} \end{bmatrix} for \quad j = 1,2,3 \tag{7}$$

where

$S_{1j} = \xi^j_y R_{21} + \xi^j_z R_{31}$, $S_{2j} = \xi^j_x R_{12} + \xi^j_z R_{32}$, $S_{3j} = \xi^j_x R_{13} + \xi^j_y R_{23}$

$R_{ij} = u_{i,\xi}\xi_{x_j} + u_{i,\eta}\eta_{x_j} + u_{i,\zeta}\zeta_{x_j}$, for $i, j = 1, 2, 3$

3 Numerical methods

3.1 Discretization

To discretize the momentum equations (6) in space, the central difference is used for the pressure and viscous terms and the second-order upwind difference for the convection terms as follows:

$$\left[U\frac{\partial u}{\partial \xi}\right]_{i,j,k} = \frac{1}{2}(|U|+U)\delta_{\xi}^{-}u_{i,j,k} - \frac{1}{2}(|U|-U)\delta_{\xi}^{+}u_{i,j,k} \tag{8}$$

$$\left[\xi_x\frac{\partial P}{\partial \xi}\right]_{i,j,k} = (\xi_x)_{i,j,k}\delta_{\xi}P_{i,j,k} \tag{9}$$

$$\left[\frac{\partial}{\partial \xi}\{\frac{\nu_t}{J}\left((\xi_x)^2+g^{11}\right)\frac{\partial u}{\partial \xi}\}\right]_{i,j,k} = \widetilde{\delta}_{\xi}\left[\frac{\nu_t}{J}\left((\xi_x)^2+g^{11}\right)\widetilde{\delta}_{\xi}u_{i,j,k}\right] \tag{10}$$

where the finite difference operators are given by

$$\begin{aligned}
\delta_{\xi}^{\pm}\phi_{i,j,k} &= \pm\frac{1}{2\triangle\xi}\left[-3\phi_{i,j,k}+4\phi_{i\pm1,j,k}-\phi_{i\pm2,j,k}\right] \\
\delta_{\xi}\phi_{i,j,k} &= \frac{1}{2\triangle\xi}\left[\phi_{i+1,j,k}-\phi_{i-1,j,k}\right] \\
\widetilde{\delta}_{\xi}\phi_{i,j,k} &= \frac{1}{\triangle\xi}\left[\phi_{i+1/2,j,k}-\phi_{i-1/2,j,k}\right]
\end{aligned} \tag{11}$$

The metrics and the Jacobian of the geometric transformation are calculated at the (i,j,k) nodes using the central difference. To compute the metrics and the Jacobian at the half nodes, a simple averaging procedure is employed. The continuity equation (5) is discretized using the central-difference approximations. The discrete divergence operator is defined as follows:

$$\mathrm{DIV}[Q_{i,j,k}] = J\delta_{\xi^k}(\frac{U^k}{J}) = 0 \tag{12}$$

where is the discrete divergence operator and Q represents the velocity vector $(u,v,w)^T$. After spatial derivatives are discretized, a four-stage Runge-Kutta scheme(Jameson and Schmidt, 1985) is applied to integrate the discretized governing equations in time as the following.

$$\mathrm{DIV}[Q^l_{i,j,k}] = 0, \qquad for \quad l=1,2,3,4 \tag{13}$$

$$Q^l_{i,j,k} = Q^n_{i,j,k} - \alpha_l\Delta t_{i,j,k}(RHS)^{l-1}_{i,j,k}, \qquad for \quad l=1,2,3,4 \tag{14}$$

where l denotes the intermediate or iteration time level between n and $n+1$ time step, the superscript n denotes the previous time step, and $\triangle t_{i,j,k}$ represents the time increment at (i,j,k)

grid point. In case of the four-stage scheme, $\alpha_1 = 1/4$, $\alpha_2 = 1/3$, $\alpha_3 = 1/2$, $\alpha_4 = 1$ and RHS denotes the discretized form of the momentum equation (6) except the time derivative term, i.e.,

$$RHS = U^k \frac{\partial u_i}{\partial \xi^k} + \xi^k_{x_i} \frac{\partial}{\partial \xi^k} P - J\left(\frac{\partial E_{v1}}{\partial \xi} + \frac{\partial E_{v2}}{\partial \eta} + \frac{\partial E_{v3}}{\partial \zeta}\right) \tag{15}$$

3.2 Velocity-Pressure coupling

If the pressure is known, the equation (14) can be employed to solve for (u, v, w). However, the pressure is not known a priori and must be determined by requiring the velocity field to satisfy the continuity equation (13). The major difficulty in calculating incompressible flows arises from the fact the continuity equation is not a time-evolution equation, but rather a constraint that is imposed to obtain a divergence-free velocity field. In the present study, the incompressibility constraint is enforced through a discrete pressure-Poisson equation, designed to eliminate the problems associated with the use of a non-staggered grid(Sotiropoulos and Abdallah, 1992).
The three scalar momentum equations given in the equation (14) can be written as follows:

$$(u_i)^l_{i,j,k} = (u_i)^n_{i,j,k} - \alpha \Delta t [f^{x_i}_{i,j,k} + (\xi_{x_i}\delta_\xi + \eta_{x_i}\delta_\eta + \zeta_{x_i}\delta_\zeta) P_{i,j,k}]^{l-1} \quad for \;\; i = 1, 2, 3 \tag{16}$$

where $f^{x_i} = (f^x, f^y, f^z)$ contains the discrete approximations of the convective and viscous terms in the ξ, η and ξ-momentum equation, respectively. To derive the discrete pressure equation, the discrete continuity equation including the artificial mass source term, given as follows, is employed.

$$DIV[Q^l_{i,j,k}] = \epsilon J(\widetilde{L} - L)[P^{l-1}_{i,j,k}] \tag{17}$$

where ϵ is a positive constant ($\epsilon < 1$), used to control the size of the source term and the operator L, $\widetilde{L}$ are defined as $L = \delta_{\xi^k}(\frac{\Delta t g^{kk}}{J}\delta_{\xi^k})$, $\widetilde{L} = \widetilde{\delta}_{\xi^k}(\frac{\Delta t g^{kk}}{J}\widetilde{\delta}_{\xi^k})$.

By substituting the momentum equations (16) into the modified discrete continuity equation (17), the following discrete pressure equation can be derived.

$$(1-\epsilon)L[P^{l-1}_{i,j,k}] + \epsilon\widetilde{L}[P^{l-1}_{i,j,k}] + N[P^{l-1}_{i,j,k}] = \frac{1}{\alpha_l} DIV[Q^n_{i,j,k}] - \sigma^{l-1}_{i,j,k} \tag{18}$$

where $N = \delta_{\xi^k}(\frac{\Delta t g^{jk}}{J}\delta_{xi^j})(k \neq j)$, $\sigma_{i,j,k} = \delta_{\xi^i}\left[\frac{\Delta t}{J}\xi^k_{x_i} f^k\right]$.
Now the discrete pressure operators couple the odd and even nodes of the pressure for the sufficiently large values of the ϵ parameter.

3.3 Boundary conditions

With the fully-elliptic momentum equations, it is necessary to specify the boundary conditions on all boundaries. In the present study, H-O type grid topology is chosen and the boundaries of the physical domain, shown in Figure 1, consist of the body surface(IJKL), the inlet plane(ABCD), the exit plane(EFGH), the symmetry center plane(AILD, JEHK, DLKHGC), the outer boundary(BFGC) and the free surface(AIJEFB). The boundary conditions are applied as follows: on the

inlet plane, $u = 1$, $v = w = 0$, $P_\xi = 0$; on the exit plane, $u_{\xi\xi} = v_{\xi\xi} = w_{\xi\xi}$, $P_\xi = 0$; on the symmetry center plane, $v = u_\zeta = w_\zeta = 0$, $P_\zeta = 0$; on the outer boundary, $u_\eta = v_\eta = w_\eta = 0$, $P_\eta = 0$ and on the hull surface, $u = v = w = 0$, $P_\eta = 0$. For the free surface boundary, exact kinematic and approximate dynamic free-surface conditions are applied on the actual free surface, which is determined as part of the solution. The derivation of these equations and the procedure for determining the free surface are described next.

The dynamic free surface condition states that the stresses are continuous across the free surface. In the present study the free surface boundary layer is not of interest, thus neglecting the existence of boundary layer very close to the free surface, velocity boundary condition on the free surface can be approximated by zero gradient extrapolation, while the piezo-metric pressure on the free surface is given as following.

$$P = \frac{-h}{F_r^2} \qquad at \;\; z = h \tag{19}$$

The kinematic boundary condition without any approximation is

$$\frac{D(h)}{Dt} = \frac{\partial h}{\partial t} + u\frac{\partial h}{\partial x} + v\frac{\partial h}{\partial y} - w = 0 \qquad on \;\; z = h(x, y, t) \tag{20}$$

where h is the free surface height. The kinematic condition in Cartesian coordinates (x, y) is transformed to general coordinates (ξ^*, η^*). Then the kinematic condition can be rewritten as follows:

$$\frac{\partial h}{\partial t} + U^*\frac{\partial h}{\partial \xi^*} + V^*\frac{\partial h}{\partial \eta^*} - w = 0 \tag{21}$$

where $U^* = \xi_x^*(u + \frac{\partial x_g}{\partial t}) + \xi_y^*(v + \frac{\partial y_g}{\partial t})$ and $V^* = \eta_x^*(u + \frac{\partial x_g}{\partial t}) + \eta_y^*(v + \frac{\partial y_g}{\partial t})$.
The downstream and the far field boundary conditions are of big concern since the reflection of the waves from these boundary ruins the interior solution. A damping function is introduced in the kinematic free surface condition to reduce the amplitude of wave approaching outer and exit boundaries. In the present method, an artificial damping function(Hino, 1994b) is added to the equation (21) and which gives

$$\frac{\partial h}{\partial t} + U^*\frac{\partial h}{\partial \xi^*} + V^*\frac{\partial h}{\partial \eta^*} - w + d(x, y)h = 0 \tag{22}$$

in which $d(x, y)$ is the damping function defined as follows:

$$d(x, y) = a \times \max(d_x(x), d_y(y)) \tag{23}$$

Also, the functions $d_x(x)$ and $d_y(y)$ are defined as

$$d_x(x) = \begin{cases} \left(\frac{x - x_d}{x_o - x_d}\right)^2 & \text{if} \quad x_d \le x \le x_o \\ 0 & \text{otherwise} \end{cases} \qquad d_y(y) = \begin{cases} \left(\frac{y - y_d}{y_o - y_d}\right)^2 & \text{if} \quad y_d \le y \le y_o \\ 0 & \text{otherwise} \end{cases}$$

where a is the parameter which controls the amount of damping and x_d, y_d is the coordinate from which the damping zone starts and x_o, y_o is the location of outflow and side boundary. The present calculation used the values of $(a, x_d, y_d) = (20, x_o - 2\pi F_r^2, 0.6y_o)$. The equation (22) is solved using the two-step Lax-Wendroff scheme. Applying the Lax-Wendroff scheme to the kinematic boundary condition, the following equations are obtained.

1st step :

$$h_{i,j}^{+} = h_{i,j}^{n} + \Delta t \left[-U^{*}(h_{i+1,j}^{n} - h_{i,j}^{n}) - V^{*}(h_{i,j+1}^{n} - h_{i,j}^{n}) + w - d(x,y)h^{n} \right]$$

2nd step :

$$h_{i,j}^{n+1} = \frac{1}{2}(h_{i,j}^{n} + h_{i,j}^{+}) + \frac{\Delta t}{2} \left[-U^{*}(h_{i,j}^{+} - h_{i-1,j}^{+}) - V^{*}(h_{i,j}^{+} - h_{i,j-1}^{+}) + w - d(x,y)h^{+} \right] \quad (24)$$

The first step, utilizing a forward difference for the spatial derivative, gives an intermediate value of $h_{i,j}$ at time level n+1, which is denoted by $h_{i,j}^{+}$, while the second step, utilizing a backward difference, then provides the final value of $h_{i,j}$ at time level n+1.

3.4 Free-Surface tracking and moving boundary fitted grid generation

In the present study, the free-surface location, not known a priori, is updated at each time step using the kinematic boundary condition and a moving boundary-fitted grid is constructed consequently so that one of the grid surfaces($\zeta = 1$) always coincides with the free surface. The present method begins with the preparation of a background grid, which is generated only once and fixed in time. The purpose of the background grid is to provide predetermined girthwise grid paths along which not only the free-surface grid points are allowed to move, but the actual computational grid points are generated by the interpolation. Once wave heights are obtained as a solution of the equation (24), the free-surface grid points are moved along the girthwise grid lines to the locations of the same wave heights. Then the grid points below the free surface are redistributed by the linear interpolation using the arc-length distribution of the computational grid at the previous time level. For the allowance of the maximum wave elevation, the background grid is constructed to cover the domain well above the undisturbed free surface and therefore a set of offsets for the hull lines above the still water level is required. For the generation of the background grid, a two dimensional grid in cross-planes(x=constant) are generated using the GRAPE method(Sorenson, 1982). Then the three dimensional grid is constructed by connecting the corresponding points of every cross-plane.

3.5 Overall solution procedure and convergence acceleration

The following steps are employed to solve iteratively the three-dimensional turbulent flow with the surface wave fields around ship models.

1. Construct the initial body-fitted coordinate system for the given body geometry and solution domain for a calm free surface.
2. Specify the initial conditions for velocity and pressure field or read from the previous solution.
3. Generate new grid system algebraically with free surface height obtained from the kinematic free surface condition, and calculate the related geometric coefficients and base vectors.

4. Specify the eddy viscosity using the modified Baldwin-Lomax model.
5. Compute f^{x_i} at the "$l-1$" stage.
6. Compute the right hand side of the pressure equation (18)
7. To obtain the pressure field at the "$l-1$" stage, solve the pressure equation (18) using the point successive relaxation method. Since the steady state of the solution is of interest, only one iteration is performed on the pressure equation
8. Compute the right hand side of the momentum equations using the already computed f^{x_i}(step 5) and the new pressure field(step 7).
9. Update the velocity field using the equation (14)
10. Calculate the free surface height based on the newly obtained velocities.
11. Try steps from 3 to 10 for the next time step until converged solution is obtained.

In the four stage Runge-Kutta scheme, the steps from 5 to 9 are repeated for $l = 1, 2, 3, 4$, since $Q^l = Q^{n+1}$ for the $l = 4$. In order to save computational time, the viscous part and pressure are updated only at the first stage of the four-stage procedure and kept constant through the subsequent three stages. To enhance the convergence rate of the time marching procedure the local time steeping and implicit residual smoothing scheme are employed in the present study. The time increment is computed and stored for every node at the beginning of marching procedure as follows:

$$\Delta t_{i,j,k} = CFL \Delta S_{i,j,k} \tag{25}$$

where $\Delta S_{i,j,k} = \min(\sqrt{g_{11}}, \sqrt{g_{22}}, \sqrt{g_{33}})$
In the above equation, CFL is the Courant-Friedrich-Lewis number and g_{11}, g_{22} and g_{33} are the components of the covariant metric tensor which represent the local arc-lengths in the ξ, η and ζ directions, respectively. Furthermore, the implicit residual smoothing scheme(Jameson and Schmidt, 1985) is used to increase the bound of the stability limit of the time stepping scheme, in which the residual is smoothed by the constant coefficient implicit operator to define a new residual:

$$(1 - \gamma_\xi \delta_{\xi\xi})(1 - \gamma_\eta \delta_{\eta\eta})(1 - \gamma_\zeta \delta_{\zeta\zeta}) \overline{RHS^l_{i,j,k}} = RHS^l_{i,j,k} \tag{26}$$

where γ_ξ, γ_η and γ_ζ are the smoothing parameter. The above equation is solved using the Thomas algorithm and the smoothed residual replaces the residual in the equation (19).

4 Numerical results and discussions

The calculations have been carried out and the results are compared with the experimental data for a Series 60 $C_B = 0.6$ ship model. The results are presented for both $F_r = 0$ and $F_r = 0.316$ to investigate the effect of the free surface on the flow. The parameters and the conditions of the computations are summarized in Table 1. The $F_r = 0.316$ is same as, but the $R_e = 4 \times 10^6$ is a little lower than, the corresponding values of the experiments(Toda et al, 1992).

Table 1: Condition of calculation

Model	Series 60	
R_e	4.0×10^6	4.0×10^6
F_r	0.000	0.316
Domain	$-0.5 \leq x/L \leq 2.0, r/L \leq 0.75$	
grid	$123 \times 51 \times 37$	
Iteration	6000	3000

In the calculation, the converged solution of the flow for $F_r = 0$ was used as an initial guess in the calculation of the flow for $F_r = 0.316$. Figure 2 shows the computed wave profile along the hull side for $F_r = 0.316$ in comparison with the experimental data. The computed profile agrees very well with the data except near the bow, where the calculation fails to capture the thin water film.

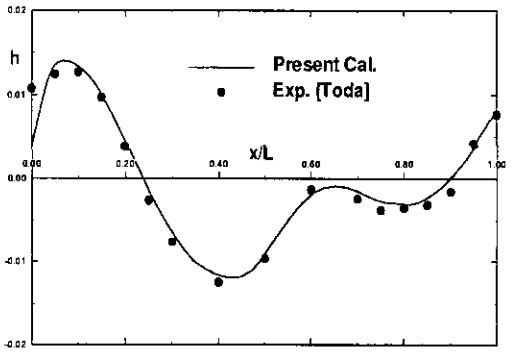

Figure 2: Wave profile along the hull surface

In Figure 3, the wave contours for $F_r = 0.316$ are shown in comparison with the measured data. Although the computed result simulates very well the measured wave patterns close to the hull, it degenerates over the region away from the hull. Note the wave elevations at the crests and the hollows are generally under- and over-predicted, respectively.

For detailed comparisons, the transverse profiles of the wave elevation are shown in Figure 4. From x/L=0 to x/L=0.4, the computed transverse wave-elevations agree well with the measured ones; at x/L=0.7, the computed wave profiles are not smooth near the hull and the positions of the crests and hollows of the bow and fore-shoulder waves are predicted incorrectly; at x/L=1.0 and x/L=1.2, the computed results fail to predict the detailed profiles of the bow and shoulder waves.

The calculated longitudinal wave profiles in Figure 5 show a good agreement with the experimental data for the cuts close to the hull, but the computational results are getting worse as the wave cut moves away from the hull. Based on the above observations, it can be judged that the present grid was not fine enough, particularly in the transverse direction, to produce an accurate solution. It is also noted the accuracy of the computed wave elevation was degraded by the proximity of the wave-damping zone on the free surface. Note the computed waves are damped rapidly

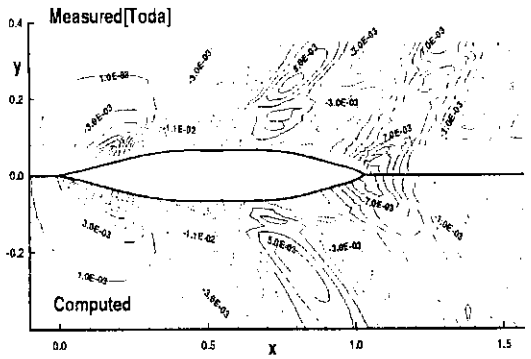

Figure 3: Comparison of contours of wave elevation

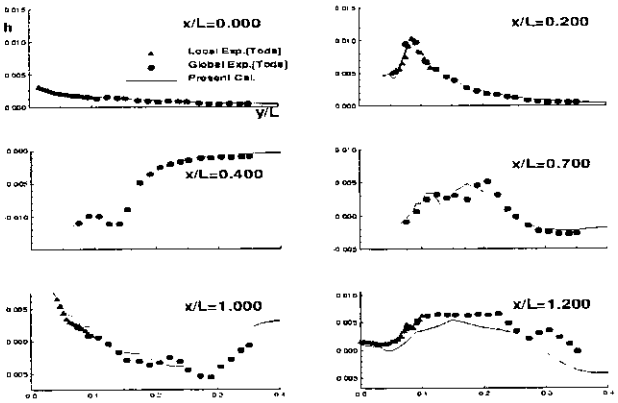

Figure 4: Transverse cut wave profiles

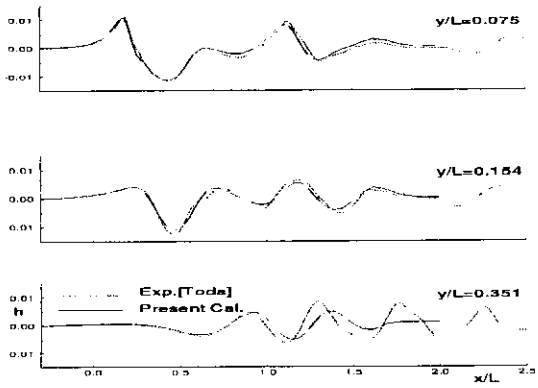

Figure 5: Longitudinal cut wave profiles

by the damping zone located at $1.5 \leq x/L \leq 2.0$.

Figures from 6 to 13 show the velocity and pressure distributions at selected stations from the bow to the near wake. In Figure 6, 8, 10 and 12, the axial velocity contours as well as the transverse vectors are shown on the left and the pressure contours on the right, in the first row for the measured data, the second for the computed results of $F_r = 0$, and the last for those of $F_r = 0.316$. In Figure 7, 9, 11 and 13, the transverse profiles of the three velocity components and the pressure coefficient are presented. The results for $F_r = 0$ are included to highlight the effects of the free surface on the flow field. In Figure 6, the computational results simulate very well the overall characteristics of the bow flow both with and without free surface effect. At x/L=0, due to the stagnation effect at the bow,

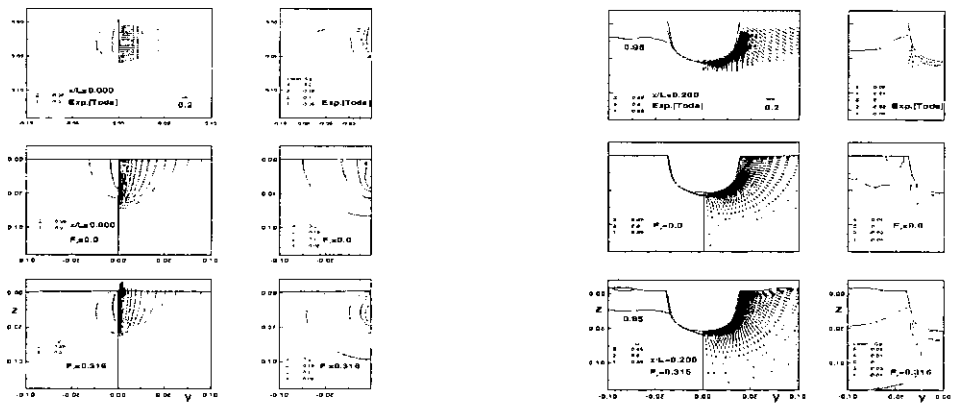

Figure 6: Comparison of longitudinal velocity, pressure and transverse vectors at x/L = 0.0 and 0.2 stations

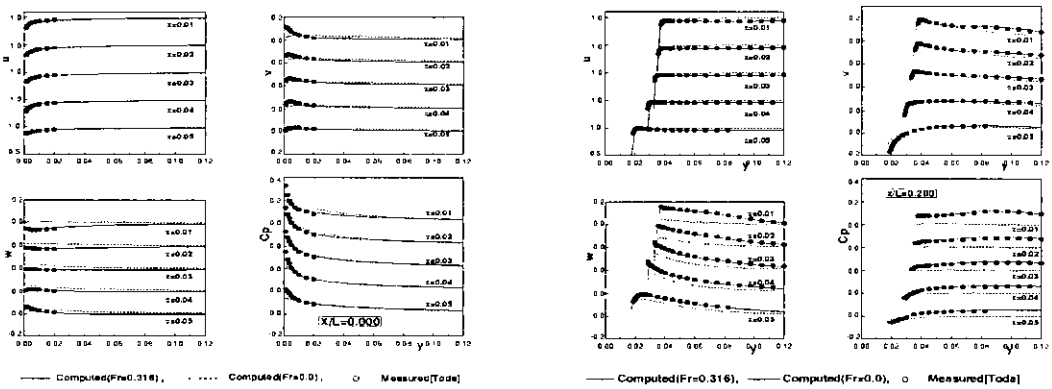

Figure 7: Velocity and pressure profiles at $x/L = 0.0$ and 0.2 stations

the transverse vectors direct away from the center and the longitudinal velocity is decelerated. For $F_r = 0.316$, the axial velocities and the pressures are respectively increased and decreased near

the free surface due to the effect of the bow wave. The transverse vectors are relatively large and directing upward near the free surface. The calculated transverse vectors are generally smaller than the measured ones although the comparison was not possible on the region very close to the free surface since the data was not available. Figure 7 shows more detailed differences of the velocity components and the pressure coefficient for the corresponding station. The differences between the computed results and the measured data are relatively large for the horizontal and vertical velocity components near the bow and the free surface. In general, the effect of the free surface diminishes as the water depth increases. At x/L=0.2, the velocities are predicted in good agreement with the data except the fact that the boundary layer thickness is predicted a little thicker at the keel and the penetration of free surface effect is slightly deeper in the calculation. For $F_r = 0.316$, a region of the retarded axial velocity is predicted near the crest of the diverging bow wave. The transverse vectors direct outward and downward due to the section area increase and the girthwise pressure gradient. Their magnitudes reach up to about 30% of the ship speed near the free surface. The pressure coefficient for $F_r = 0.316$ is generally higher than that for $F_r = 0$ due to the bow wave. The low pressure region is predicted near the round bilge but the pressure level is higher than the measurement. The profiles in Figure 7 show a good agreement and display clearly the effect of the wave on the velocity and the pressure. Again, the effect of the free surface reduces as the water depth increases but the reduction of the free-surface effect appears much slower for the pressure and the vertical velocity. In Figure 8, as the axial velocity distribution over the side hull is reasonably predicted, so is the boundary layer thickness at x/L=0.4. But the boundary layer thickness near the keel is predicted a little thicker than the measurement.

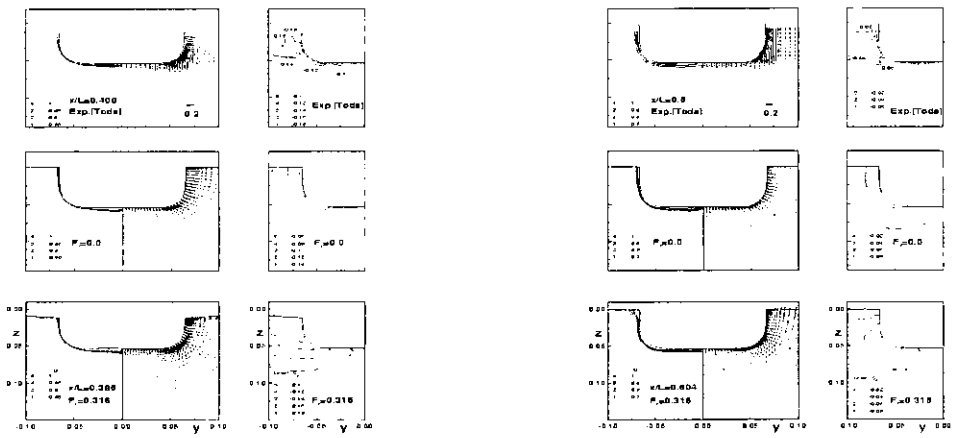

Figure 8: Comparison of longitudinal velocity, pressure and transverse vectors at x/L = 0.4 and 0.6 stations around midship

The transverse vectors direct still outward and downward but their magnitudes are much smaller than those at the x/L=0.2 station. The smaller transverse vectors may be related to the adverse pressure gradient in the girthwise direction which was favorable at x/L=0.2. The calculated transverse vectors near the hull are different from the experimental data particularly from the bilge to the keel. The reason for this difference is not known but it may be associated with the difference of the boundary thickness mentioned above. The pressure for $F_r = 0.316$ is much lower

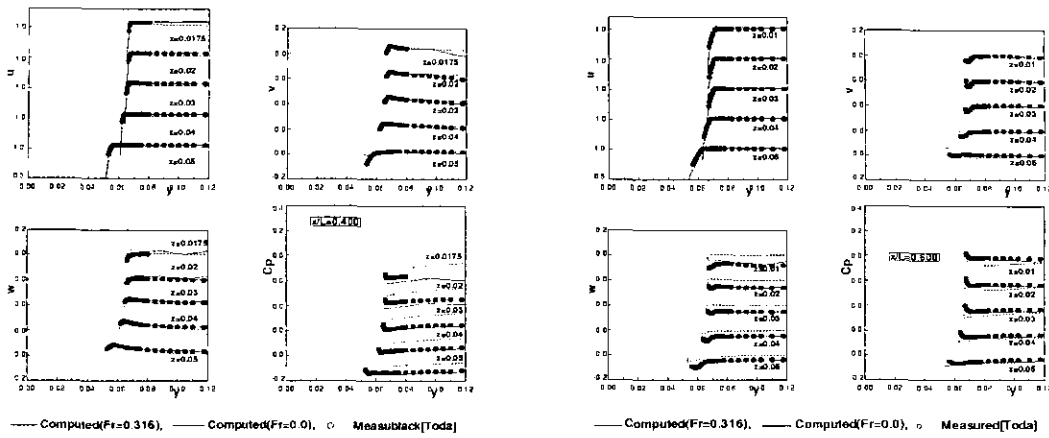

Figure 9: Velocity and pressure profiles at $x/L = 0.4$ and 0.6 stations

than that for $F_r = 0$ due to the effect of the trough of the fore-shoulder wave. The contours of low pressures on the hull side show the difference between the computed results and the measured data. The computed profiles at x/L=0.4 in Figure 9 show a good agreement with the experimental data except near the free surface where the measured pressure is higher than the computed result. This may be due to the inaccuracy of the calculation, but it is possible the measured data very close to the hull surface was influenced by the interference between the probe and the hull. At x/L=0.6, which is close to the after-shoulder wave crest, the boundary layer thickness is more or less uniform along the girth. In the computation, however, the boundary layer is abruptly thickened very close to the free surface. This could not be confirmed in the experiment since there was no velocity measurement available. This rapid thickening of the boundary layer is consistent with the convergence of the limiting surface streamlines to the free surface which is relatively flat and undisturbed at x/L=0.6. The transverse vectors direct generally upward and those near the hull direct from the keel to the bilge and to the free surface. The computed pressure contours show a poor agreement with the measured ones. The pressure is calculated lower than the data especially close to the hull. More detailed differences between the calculated and the measured velocity and pressure are presented in Figure 9. The vertical velocity for $F_r = 0.316$ is much smaller than those for $F_r = 0$. On the contrary the pressure coefficient for $F_r = 0.316$ is larger but the difference decreases as the water depth increases.

In Figure 10, the computation simulates the characteristics of the axial velocity contours including the bulges at the mid-girth position. But the boundary layer is computed a little thicker near the bulges and thinner over the bilge to the bottom. The transverse vectors directs from outside to the hull which show the convergence of the streamlines due to the decrease of the sectional area of the ship model. The formation of the bilge vortex can be traced from the transverse vectors around the bilge area where the pressure coefficient contours show low pressures. This low pressure region is computed smaller and bigger than that of the double body(F_r= 0) at x/L=0.8 and x/L=0.9 respectively, which suggests the strength of the bilge vortex may be influenced by the free-surface. The velocity profiles for x/L=0.8 and x/L=0.9 in Figure 11 show a poor agreement with the experimental data. Note the magnitudes of all three velocity components are predicted

generally smaller inside the boundary layer but the pressure is predicted relatively well. In Figure 12, the characteristics of the stern and near wake flows are reasonably simulated in qualitative sense. However, the computed velocities near the bilge vortex, which is predicted much weaker and more elongate vertically in the calculation, are different from the data. Again the velocities inside the boundary layer are predicted smaller particularly near the free surface where the thickness of the shear layer is large.

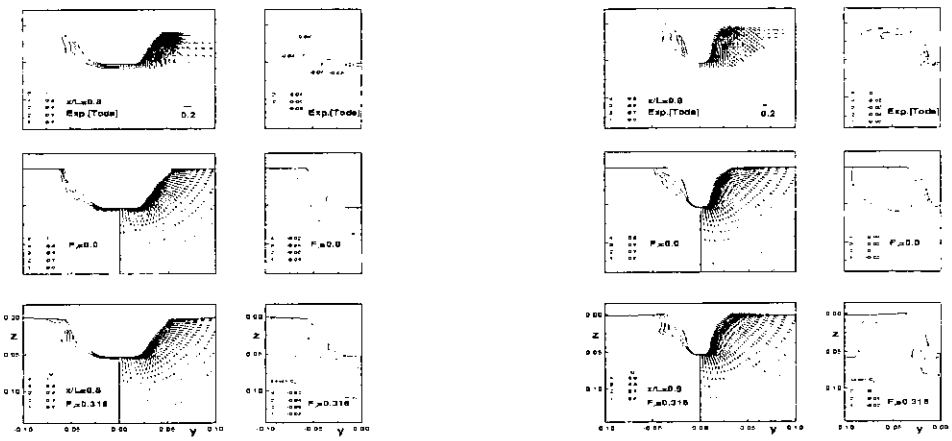

Figure 10: Comparison of longitudinal velocity, pressure and transverse vectors at $x/L =$ 0.8 and 0.9 stations

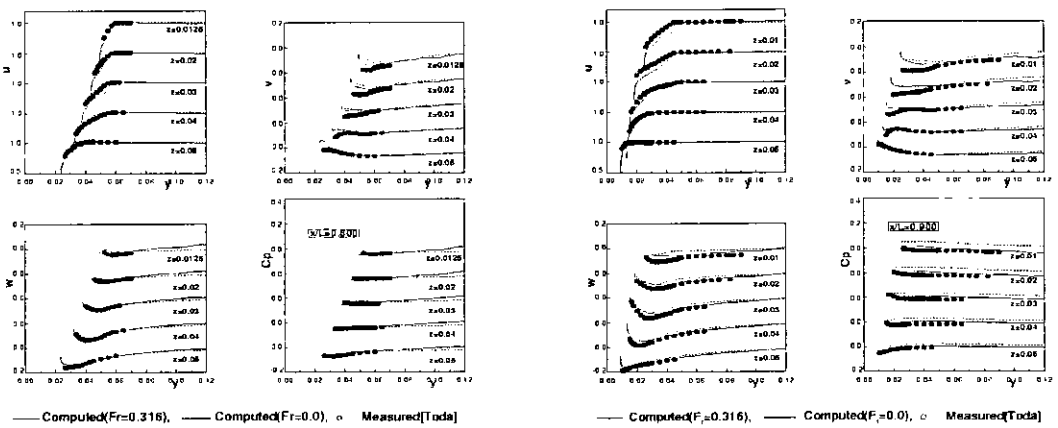

Figure 11: Velocity and pressure profiles at $x/L = 0.8$ and 0.9 stations

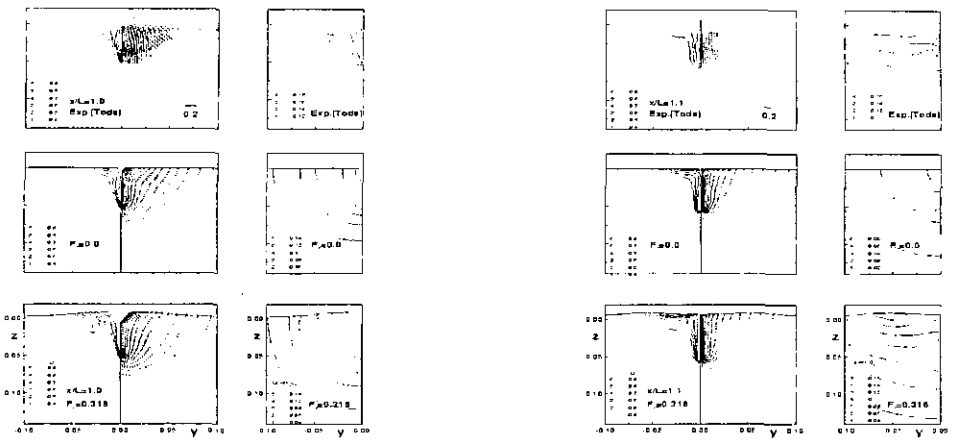

Figure 12: Comparison of longitudinal velocity, pressure and transverse vectors at x/L = 1.0 and 1.1 stations

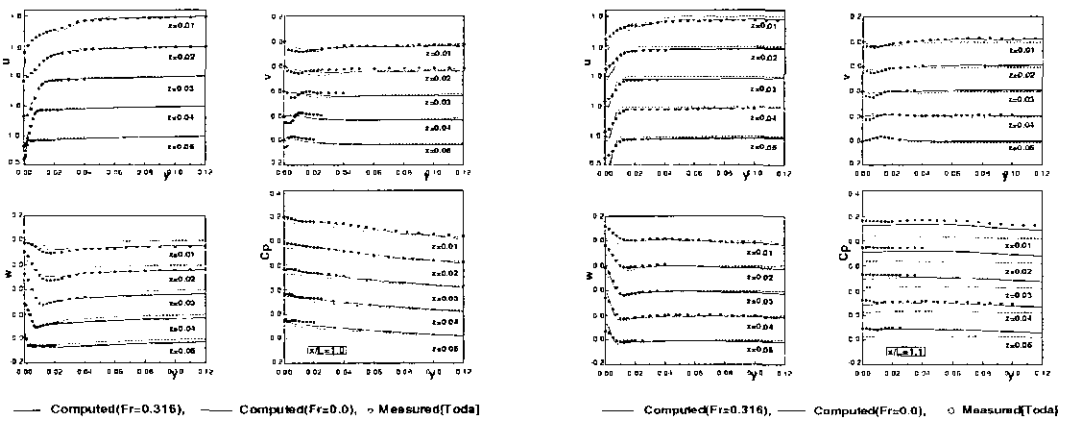

Figure 13: Velocity and pressure profiles at x/L = 1.0 and 1.1 stations

In Figure 13, the discrepancy of the horizontal velocity profiles is not small close to the location of the bilge vortex. The pressure profiles show a reasonably good agreement at x/L=1.0 but depict an overall underprediction at x/L=1.1.

The longitudinal distributions of the sectional pressure and friction resistance coefficients for F_r= 0 and 0.316 are given in Figure 14. Because of the free-surface effect, the pressure resistance(R_{pg}) increases over the bow and stern parts of about 20% the ship length, while it decreases over the middle. Similarly, the friction resistance(R_{fg}), which is almost constant from the bow to the stern, slightly increases over the forebody of 30% and the afterbody of 20% the ship length but slightly decreases over the middle. The resistance for F_r= 0.316 is much larger than F_r= 0 due to mainly the increase in the pressure resistance over the bow part.

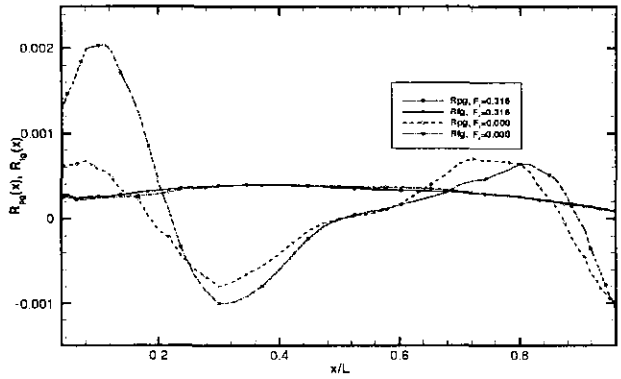

Figure 14: An example of manual-nesting using parametric macro

Table 2: Comparison of computed and measured ship resistance coefficients

Model	Condition	$R_e \times 10^{-6}$	F_r	$C_F \times 10^{-3}$	$C_P \times 10^{-3}$	$C_T \times 10^{-3}$
Series 60	Measured	4.34	0.316	3.522		5.959
($C_B = 60$)	Computed	4.000	0.316	3.497	2.109	5.606

Finally, the estimated resistance coefficients are given in Table 2 with the experimental data. The friction resistance is underestimated by about 1% and the total resistance is underestimated by 6% when they are compared with the measured values. Note the Reynolds Number of the computation is a little lower than that of the experiment while the Froude number is same as the experiment.

5 Conclusion

A RANS solver for the calculation of the turbulent flow around a surface ship model including the free-surface effects has been evaluated through the comparisons with detailed experimental data. Based on the results of the present study, the following conclusions are drawn. The present solver is capable of simulating the flow around a ship model including the free-surface waves. The computational results for Series 60 C_B=0.6 ship model show generally good agreements with the experimental data. However, the velocities of the stern and the near wake and the free-surface waves in regions away from the hull are not accurately calculated. The comparisons between the computed results for F_r= 0 and F_r= 0.316 suggest that the inclusion of free-surface effects could be important for realistic simulations of the flow around a surface ship model at non-zero Froude numbers. The improvements of the grid resolution, the accuracy of the numerical schemes especially for the free-surface treatment, and the turbulence modeling seem to be essential for more accurate computational results.

References

CHIMA, R.V., GIEL, P.W. AND BOYLE, R.J. 1993 An Algebraic Turbulence Model for Three-Dimensional Viscous Flows. NASA Technical Memorandum 105931

HINO , T. 1994b Computations of Free Surface Flows around a Ship Hull by a Multigrid NS Solver. Proc. Workshop on Wave Resistance and Viscous Flow(Univ. of Tokyo, Japan)

JAMESON, A. AND SCHMIDT, W. 1985 Some Recent Developments in Numerical Methods for Transonic Flows. Computer Methods in Applied Mechanics. and Eng., **51**

KIM, J.J. AND KIM, H.T. 2000 Computation of Turbulent Flow around a Ship Model with Free-Surface. (submitted for publication to J. of Society of Naval Architects of Korea).

PROCEEDINGS, CFD WORKSHOP TOKYO 1994, **1-2**

SORENSON, R.L. 1982 Grid Generation by Elliptic Partial Differential Equations for a Tri-Element Augmentor-Wing Airfoil. Numerical Grid Generation (ed. Thompson, J. F.)

SOTIROPOULOS, F. AND ABDALLAH, S. 1992 A Primitive Variable Method for the Solution of Three-Dimensional Incompressible Viscous Flows. JCP, **103**

SUNG, C.H., TSAI, J.F., HUANG, T.T. AND SMITH, W.E. 1993 Effects of Turbulence Models on Axisymmetric Stern Flows Computed by an Incompressible Viscous Flow Solver. Proc. 6th International Conference on Numerical Ship Hydrodynamics, Iowa City, IA, U.S.A)

TAHARA, Y. AND STERN, F. 1996 A Large Domain Approach for Calculating Ship Boundary Layers and Wakes and Wave Fields for Nonzero Froude Number. JCP, **127**

TODA, Y., STERN, F. AND LONGO, J. 1992 Mean-Flow Measurements in the Boundary Layer and Wake and Wave Field of a Series 60 C_B=0.6 Ship Model - Part 1: Froude Numbers, 0.16 and 0.316. J. of Ship Research, **37**